Co-published by
Institute of Fluid-Flow Machinery
Polish Academy of Sciences
Committee on Thermodynamics and Combustion
Polish Academy of Sciences

http://www.imp.gda.pl/archives-of-thermodynamics/

ARCHIVES OF THERMODYNAMICS

Convective Transfer Analysis of Magnetised Ternary Hybrid Nanofluid over a Linear Stretching Sheet: Non-Similar Solutions

Ahmed Jan[a*], Farida Aslam[b], Rubina Adnan[c]

[a]College of Mechanical and Electronic Engineering, Shandong University of Science and Technology, Qingdao, Shandong Province, 266590, PR China
[b]Department of Mathematical Science, BUITEMS, Quetta 87300, Pakistan
[c]Department of Computer Science, COMSATS University Islamabad, Pakistan
*Corresponding author email: ahmedjan400@gmail.com; jan_ahmed@sdust.edu.cn

Received: 21.11.2025; revised: 13.04.2026; accepted: 22.04.2026

Abstract

Use of nanofluids to improve heat transfer properties has drawn considerable concern due to their wide use in various applications such as electronic appliances, fuel cell batteries and hybrid-powered engines. These are only a few examples of the many applications of heat transfer that can greatly utilise the distinctive properties of nanofluids. A magnetohydrodynamic nanofluid convective study is carried out for a sheet stretched under a non-uniform heat source/sink in a permeable medium. The heat transfer analysis simulations entail dissipation of porosity and the presence of Ohmic heating. Non-similarity transformations are then applied to the equations that have been formulated to derive dimensionless partial differential equations. Local non-similarity approach has been used to transform partial differential equations into an equation where partial differential equations can be solved as ordinary differential equations, using the bvp4c MATLAB tool. Every physical parameter is represented in a graphical representation. Moreover, the tables that present the summary of the skin friction coefficient and Nusselt number are evaluated in detail. The main findings of this study include the fact that an increase in the strength of the magnetic field decreases the fluid velocity but improves the thermal distribution. It has been observed that the higher the porosity, the lower the skin friction. In addition, high radiation levels also help in having a more favourable temperature field.

Keywords: Non-similar analysis; Non-uniform heat source/sink; Magnetohydrodynamic; Thermal radiation; MATLAB bvp4c.

Vol. 47(2026), No. 2, 141–150; doi: 10.24425/ather.2026.158680

Cite this manuscript as: Jan, A., Aslam, F., & Adnan, R. (2026). Convective Transfer Analysis of Magnetised Ternary Hybrid Nanofluid over a Linear Stretching Sheet: Non-Similar Solutions. *Archives of Thermodynamics*, 47(2), 141–150.

1. Introduction

There have already been extensive studies designed to analyse the thermo-physical properties of traditional heat transfer fluids, but these fluids are not sufficient to handle the increased challenges that are presented by contemporary technology. As a result, the introduction of nanoparticles to these fluids has been suggested as one of the solutions. Engineered composites (nanofluids) created by the mixing of nanoparticles with a base fluid have emerged as a result. Nanoparticles, which are significantly smaller than the base fluid, are added to the base fluid. Recent experimental studies show that thermal conductivity is increased significantly when nanoparticles are incorporated into conventional fluids. The outstanding natural properties of nanofluids form a bridge between the microscopic and macroscopic molecular structures. Nanofluids cannot be compared with others in terms of heat transmission. It is through their good properties that they have become a hot commodity in various industries

Nomenclature

a – time constant, 1/s
B_o – applied magnetic field, kg/(A·s^2)
C_f – skin friction
c_p – specific heat, m^2/(s^2·K)
Ec – Eckert number, $\mathrm{Ec} = (al)^2/(c_p)_f(T_w - T_\infty)$
E* – internal heat production
f, *g*, *h* – dimensionless dependent variables
F* – internal heat absorption
g – gravitational acceleration, m^2/s
Gr – Grashof number, $\mathrm{Gr} = \beta_f g(T_w - T_\infty)l^3/\nu_f{}^2$
k – thermal conductivity, W/(m·K)
k_p – permeability of free space, m^2
k^* – radiation absorption coefficient, 1/m
M – magnetic number, $M = \sigma_f B^2/a\rho_f$
Nu – Nusselt number
Pr – Prandtl number, $\mathrm{Pr} = \alpha_f/\nu_f$
q''' – heat source, W/m^3
q_r – thermal radiation, W/m^2
R_d – radiation parameter, $R_d = 4\sigma^* T_\infty^3/K_f k^*$
Re – Reynolds number, $\mathrm{Re} = al^2/\nu_f$
T – temperature, K
T_w – wall temperature, K
T_∞ – ambient temperature, K
u, *v* – velocities, m/s
x, *y* – independent variables, m

Greek symbols

α – mixed convection parameter, $\alpha = \mathrm{Gr}/\mathrm{Re}$
α_f – thermal diffusivity, m^2/s
β_f – thermal expansion, 1/K
θ – dimensionless temperature
λ – porosity parameter, $\lambda = \nu_f/k_p a$
ξ, η – non-similarity and pseudo variable
μ_f – dynamic viscosity, kg/(m·s)
ν_f – kinematic viscosity, m^2/s
ρ_f – density, kg/m^3
σ^* – Stefan-Boltzmann constant, W/(m^2·K)

Subscripts and Superscripts

f – base fluid
thnf – ternary hybrid nanofluid

Abbreviations and Acronyms

MHD – magnetohydrodynamics
ODE – ordinary differential equation
PDE – partial differential equation

such as fuel cells, electronics and hybrid engines. Moreover, nanofluids are also used in industries due to their high levels of production of quality oils and lubricants. Choi and Eastman [1] first suggested the notion of nanoparticles while conducting classic research on nanofluids, which they characterised as tailored nanoparticle suspensions in standard heat transfer fluids. It has been demonstrated that the efficiency of traditional fluids in heat transfer can be significantly enhanced by the introduction of nanoparticles. Nanofluid thermal properties were widely researched by Buongiorno [2], who prepared a whole theoretical basis to accomplish the aim. The detailed mathematical study by Mabood et al. [3] on heat transfer in the nanofluid movement in a nonlinear sheet stretching in the boundary layer is very comprehensive. The experiment was carried out considering the influence of an external magnetic field. Saddiqui et al. [4] investigated the characteristics of thermal transport under the circumstances of constant movements of the boundary layer over a stretched melting boundary. The dissipation effects in the viscous viscosity were considered in the effort. Masood et al. [5] explored stagnation point flow patterns in a hybrid nanofluid that comprised polystyrene and titanium dioxide particles suspended in water. Heat production and uptake were evaluated in an extensive manner. Hussain et al. [6] studied combined heat and mass transport via the Cross fluid framework. The probe was used to light up the input of the magnetic dipole to the motion of ferrofluid on a hard surface.

Mixed convection is prevalent across a broad spectrum of engineering, industrial and natural systems where forced and free convection processes operate concurrently. These low-velocity flow scenarios are encountered in a variety of practical applications, such as heat exchangers, marine environments, atmospheric currents, solar receivers exposed to wind, fan-cooled electronic components, and nuclear reactors during emergency shutdown scenarios. Chen et al. [7] conducted an investigation into the characteristics of laminar forced convective flow and heat transfer over a horizontal flat plate, utilising analytical methods rooted in local similarity and local non-similarity solutions to assess the impacts of streamwise pressure gradients induced by buoyancy. Chamkha et al. [8] studied coupled heat and mass transfer boundary-layer free convection over a vertical flat plate in a fluid-saturated porous medium, considering thermophoretic particle deposition and heat generation/absorption. Ahmad and Pop [9] analysed the boundary layer flow of nanofluids over a vertical flat plate embedded within a porous medium, focusing specifically on the performance of different nanoparticle varieties, including copper, alumina and titanium oxide. Mahanthesh et al. [10] explored how viscous dissipation and nonlinear thermal radiation affect the magnetohydrodynamic boundary layer flows of specific nanofluids. Cao et al. [11] studied the combined influences of nonlinear thermal radiation and partial slip conditions on the mixed convective boundary layer flow involving ternary hybrid nanoparticles of different sizes dispersed in nanofluids. Additionally, Jakeer et al. [12] carried out experiments to examine the effect of radiation on a flat sheet under nonlinear Darcy-Forchheimer flow conditions, with their research encompassing ternary hybrid nanofluids, water-based nanofluids and hybrid nanofluids.

Flow and heat transport in porous media have wide applications in various areas of science and engineering. Applications of porous media have been widely utilised in many industries, such as soil salts leaching, chemical-based catalytic reactors, grain preservation, heat exchange between soil and the atmosphere, solar energy harvest, electrochemical processes, thermal insulation of nuclear reactors, moisture diffusion in fibrous insulating media, regenerative heat exchangers, geothermal systems, and others. A large amount of literature is available on these scenarios, mostly in the classical Darcy flow situation. However, at high flow rates or in porous media with high permeability, a non-linear Darcy law effect occurs, in which inertial effects are now of interest. The effect of departure is attributed to the fact that flow separation in the medium occurs and is observable when the Reynolds number exceeds 1. It has been found that the effect of non-Darcy phenomena on natural convection in porous materials is of interest, and experimental studies have investigated a wide range of governing parameters and used various combinations of fluids and solids. Laurait and Prasad [13] examined the free convection influenced by the boundary conditions in a vertical enclosure. Recently, Beckermann and co-authors [14] carried out a numerical study in which the Forchheimer-Brinkmann extended Darcy equation of motion was used. Cortell [15] was able to explore the dynamics of fluid flow when the surfaces were impermeable, with an internal heat source or absorption and surface distension. Salahuddin et al. [16] investigated the effect of a porous medium on nanofluid flow mixed convection near an exponentially contoured surface. Two base fluids, such as water and ethylene glycol, and alumina nanoparticles were considered. Hussain et al. [17] performed an analysis of the influence of nanofluid using the Darcy-Forchheimer Casson fluid model of a stretching sheet. The aim of a numerical analysis that was carried out by Keshavarzian and Sayehvand [18] was to assess the precision of the local thermal non-equilibrium concept and the Forchheimer-Brinkman extended Darcy model.

The study of magnetohydrodynamic (MHD) flow and heat transfer across a fixed or movable planar surface has evolved as a popular research topic with several applications in a variety of technical areas, including the petroleum industry, plasma studies, geothermal energy extraction and aerodynamics. A number of artificial solutions aimed at achieving this objective have been developed since effective control of boundary layer behaviour is a crucial component. Sparrow and Cess [19] investigated the influence of an induced magnetic field on free convection heat transfer from an isothermal plate. Ellahi et al. [20] examined entropy generation and slip effects in the context of MHD heat transfer over a flat plate. Jan et al. [21] assessed heat and flow transfer analysis of magnetised nanofluid flow over a curved geometry. Iqbal and Abbasi [23] evaluated entropy generation impacts on multi-layered peristaltic flow of a curved nanofluid. The evaluation incorporated temperature-sensitive thermal conductivity traits from a Carreau-Yasuda nanofluid. Ghasemi et al. [23] examined nanofluid dynamics over an extending surface amid radiation and magnetic influences. The examination applied a distinct spectral relaxation method. Iqbal et al. [24] determined that MHD, alongside a revised Darcy's law, alters Powell-Eyring nanofluid conveyance inside a bent channel under a radial magnetic field.

This paper concentrates on the thermal characteristics of a ternary hybrid nanofluid, which is a novel arrangement that exceeds the conventional mono and hybrid nanofluids with the application of highly improved thermal conductivities and viscosities. This is attributed to synergistic blending of three kinds of nanoparticles, such as aluminium oxide Al_2O_3, titanium dioxide TiO_2 and magnesium oxide MgO, which are suspended in a liquid water base of ethylene glycol, and hence enhances the overall thermo-physical properties of the mixture, such as the density, specific heat and rheology.

The heat transfer enhancement rates in this ternary hybrid nanofluid, particularly its behaviour to nonuniform heat source/sink effects in a magnetised mixed convection boundary layer flow over an extending surface, are analysed. The greatest novelty of the study is using a nonuniform heat source, in the form of a spatially varying thermal generation term (e.g. quadratic or exponential distribution), which makes the heat flux distribution conditions much more realistic in the advanced engineering of the real world (solar collectors, nuclear reactors, electronic cooling systems, etc.). In comparison with the earlier study in which most of the literature either considered a uniform source of heat or an isolated binary nanofluid to steady thermal loading, this study is the first study to couple the nonuniform sources of heat with the complex interaction of thermo-physical processes in a ternary hybrid nanofluid to uncover the effects of perturbations due to nanoparticles on local temperature gradients and Lorentz force interactions in the magnetic forcing of the fluid. This interaction not only improves convective heat dissipation, but it also gets rid of possible hotspots that provide us with new information on how to make things more stable and efficient in mixed thermal settings. A thorough treatment of such phenomena must employ non-similarity transformations [25−29] to reduce the governing partial differential equations to a system of dimensionless ordinary differential equations that are solved numerically with the bvp4c solver of MATLAB to solve high-fidelity problems in the standard form of a boundary value problem. The physical observations, including velocity profiles, temperature distributions, skin friction coefficients and change in Nusselt number (Nu), are explained through detailed graphical plots and table representation, which elucidate the transformational quality of this hybrid solution considering the next-generation thermal management technology.

2. Problem formulation

This study examines two-dimensional incompressible boundary layer flow of a ternary hybrid nanofluid under nonuniform heat source/sink effects near an extending sheet. The flow domain is limited to $x \geq 0$ and $y \geq 0$, while the sheet resides at $y = 0$. The x-coordinate follows the sheet extension path. The y-coordinate runs perpendicular to the surface. Equal opposing forces along the x-axis extend the sheet and preserve the origin. Boundary layer approximations balance normal stress against shear stress in magnitude. A transverse magnetic field acts on the fluid. The energy equation integrates linear thermal radiation via the Rosseland diffusion model. The fluid's magnetic Reynolds number (Re) stays sufficiently low to neglect the Hall effect and induced magnetic field. The momentum equation accounts for both electric and magnetic field influences. Equations for motion and energy conservation explain mixed convection inside the boundary layer using the Boussinesq approximation, which is consistent with the specified physical framework.

A schematic flow diagram is shown in Fig. 1.

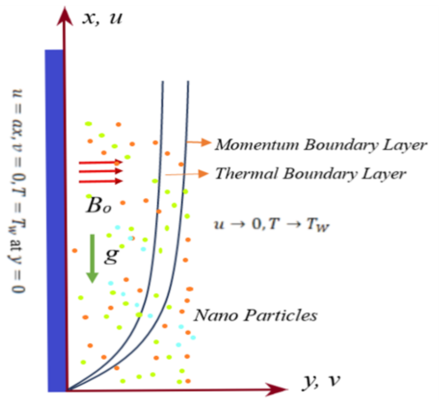

Fig. 1. Schematic flow diagram.

The set of governing equations is written as:

$$\frac{\partial u}{\partial x}+\frac{\partial v}{\partial y}=0, \tag{1}$$

$$u\frac{\partial u}{\partial x}+v\frac{\partial u}{\partial y}=\frac{\mu_{thnf}}{\rho_{thnf}}\frac{\partial^2 u}{\partial y^2}+\frac{g(\rho\beta)_{thnf}}{\rho_{thnf}}(T-T_\infty)+$$
$$-\frac{\mu_{thnf}}{\rho_{thnf}}\frac{u}{k_p}-\frac{\sigma_{thnf}B_0^2}{\rho_{thnf}}u, \tag{2}$$

$$u\frac{\partial T}{\partial x}+v\frac{\partial T}{\partial y}=\frac{k_{thnf}}{(\rho c_p)_{thnf}}\frac{\partial^2 T}{\partial y^2}-\frac{1}{(\rho c_p)_{thnf}}\frac{\partial q_r}{\partial y}+\frac{\mu_{thnf}}{(\rho c_p)_{thnf}}\left(\frac{\partial u}{\partial y}\right)^2+$$
$$+\frac{1}{(\rho c_p)_{thnf}}\left(\sigma_{thnf}B_0^2+\frac{\mu_{thnf}}{k_p}\right)u^2+\frac{q'''}{(\rho c_p)_{thnf}}, \tag{3}$$

with boundary conditions [28]:

– at $y \to 0$:

$$u=u(w)=ax, \quad v=0, \quad T=T_w, \tag{4a}$$

– as $y \to \infty$:

$$u \to 0, \quad v \to 0, \quad T \to T_\infty . \tag{4b}$$

In this model, the dynamic viscosity is μ_f, ρ_f is the fluid density, heat capacitance is $(\rho c_p)_f$; T_w, T_∞ are the free stream and ambient temperature, respectively; T is the temperature, and

$$Q'''=\frac{k_{thnf}}{x\nu_{thnf}}[E^*(T_w-T_\infty)\ +u(w)F^*(T-T_\infty)],$$

$$q_r=\frac{4\sigma^*}{3k^*}\frac{\partial T^4}{\partial y},$$

where E^* and F^* are characteristics of internal heat production and absorption that vary with space and temperature [30]. It is observed that when $E^* > 0$ and $F^* > 0$, internal heat is being produced.

3. Coordinate transformation

The coordinate transformation is used to transform the equations of fluid flow and heat transfer between the physical domain and a computational or dimensionless domain. The method enables the equations to be reformulated into a more straightforward and tractable form to improve numerical accuracy and stability. The transformation characterises a correlation between the physical coordinates and a fresh group of coordinates which are more illustrative of the geometry or flow attributes of the issue. It allows scaling of variables such as length, velocity and temperature to relevant reference quantities, thereby assisting in the generalisation of the results to varying physical conditions. It is especially applicable in curved geometries or complicated configurations of boundaries, where it is hard to formulate these problems in physical coordinates. The main characteristics of coordinate transformation are that it can lessen the number of variables, remove any dependence on the dimensions, and that it can be used to apply the boundary conditions on irregular surfaces easily. It also enables a better understanding of the governing parameters. This method, as opposed to similarity transformations, does not lose the complete dependence of the variables on both spatial coordinates, which gives a more detailed description of the flow field without any restrictive assumptions. The following transformation is introduced:

$$\eta=y\sqrt{\frac{a}{\nu_f}},\ \xi=\frac{x}{l},\ u=ax\frac{\partial f}{\partial \eta},\ v=-\sqrt{a\nu_f}\ \left(f+\xi\frac{\partial f}{\partial \xi}\right), \tag{5}$$

$$\theta(\xi,\eta)=\frac{T-T_\infty}{T_w-T_\infty}.$$

Using Eq. (5), Eq. (1) is identically satisfied. Eqs. (2)−(4) in a dimensionless non-similar system are given below:

$$\frac{\partial^3 f}{\partial \eta^3}-\left(\lambda+M\frac{\mu_f}{\mu_{thnf}}\frac{\sigma_{thnf}}{\sigma_f}\right)\frac{\partial f}{\partial \eta}+\frac{\mu_f}{\mu_{thnf}}\frac{(\rho\beta)_{thnf}}{(\rho\beta)_f}\xi^{-1}\alpha\theta+$$
$$+\frac{\rho_{thnf}}{\rho_f}\frac{\mu_f}{\mu_{thnf}}f\frac{\partial^2 f}{\partial \eta^2}-\frac{\rho_{thnf}}{\rho_f}\frac{\mu_f}{\mu_{thnf}}\left(\frac{\partial f}{\partial \eta}\right)^2=$$
$$=\frac{\rho_{thnf}}{\rho_f}\xi\left(\frac{\partial f}{\partial \eta}\frac{\partial^2 f}{\partial \xi\partial \eta}-\frac{\partial f}{\partial \xi}\frac{\partial^2 f}{\partial \eta^2}\right), \tag{6}$$

$$\frac{1}{\mathrm{Pr}}\left(\frac{k_{thnf}}{k_f}+R_d\right)\frac{\partial^2\theta}{\partial \eta^2}+\mathrm{Ec}\xi^2\frac{\mu_{thnf}}{\mu_f}\left(\frac{\partial^2 f}{\partial \eta^2}\right)^2+$$
$$+\mathrm{Ec}\xi^2\left(\lambda\frac{\mu_{thnf}}{\mu_f}+M\frac{\sigma_{thnf}}{\sigma_f}\right)\left(\frac{\partial f}{\partial \eta}\right)^2+\frac{(\rho c_p)_{thnf}}{(\rho c_p)_f}f\frac{\partial\theta}{\partial\eta}+$$
$$+\frac{k_{thnf}}{k_f}\frac{\rho_{thnf}}{\rho_f}\frac{\mu_f}{\mu_{thnf}}\frac{\mathrm{Ec}}{\mathrm{Pr}}\left[E^*\frac{\partial f}{\partial \eta}+F^*\theta\right]=$$
$$=\frac{(\rho c_p)_{thnf}}{(\rho c_p)_f}\xi\left[\frac{\partial f}{\partial \eta}\frac{\partial\theta}{\partial\xi}-\frac{\partial f}{\partial \xi}\frac{\partial\theta}{\partial\eta}\right]. \tag{7}$$

Non-similar boundary conditions are:

– at η =0:

$$\partial f/\partial\eta=1, \quad f=0, \quad \theta=1, \tag{8a}$$

– as $\eta \to \infty$:

$$\partial f/\partial\eta \to 0, \quad \theta \to 0. \tag{8b}$$

4. Physical quantities

The surface friction coefficient C_f and the local Nusselt number Nu are defined as:

$$C_f\ =\left(\frac{\tau_w}{\rho_f(u_w)^2}\right)_{y=0},\quad \mathrm{Nu}\ =\left(\frac{xq_w}{k_f(T_w-T_\infty)}\right)_{y=0}, \tag{9}$$

where τ_w is the surface shear stress, q_w is the surface heat flux:

$$\tau_w\ =\left(\mu_{thnf}\frac{\partial u}{\partial y}\right)_{y=0},\ q_w\ =-\left(\frac{k_{thnf}}{k_f}+q_r\right)\left(\frac{\partial T}{\partial y}\right)_{y=0}. \tag{10}$$

The dimensionless forms of C_f and Nu_x are:

$$\left.\begin{aligned}\mathrm{Re}^{\frac{1}{2}}C_f &= \xi^{-1}\frac{\mu_{thnf}}{\mu_f}\frac{\partial^2 f}{\partial\eta^2}(\xi,0)\\ \mathrm{Re}^{-\frac{1}{2}}\mathrm{Nu} &= -\xi\left(\frac{k_{thnf}}{k_f}+R_d\right)\frac{\partial\theta}{\partial\eta}(\xi,0)\end{aligned}\right\}. \tag{11}$$

5. Local non-similarity method

To avoid complications caused by the introduction of spatial coordinates into the physical controlling parameters, a stream-wise coordinate must be introduced. The addition of these coordinates will help eliminate unnecessary variables from the flow equations. Applying the strategy described in Sparrow et al. [25] and Sparrow and Yu [26] modifies the local flow problem of similarity into a non-similar flow problem. In addition, the authors formulated the two-equation truncation model in this notion while considering the impact of the stream-wise coordinate [31,32]. In certain research, including the stream-wise coordinate has been shown to significantly improve the flow and mass balance, whereas in others, including this coordinate has not yet been shown to make a substantial improvement. Upon applying the Taylor series expansion, all terms containing $\partial/\partial\xi$ in Eqs. (6)–(8) are eliminated. This enables the introduction of necessary variables and the formulation of first- and second-level truncation equations.

5.1. First-level truncation

Assuming that $\xi \ll 1$, the right-hand sides of Eqs. (6)−(8) are equal to zero. Equations (6)−(8) can be rewritten as:

$$f''' - \left(\lambda + M\frac{\mu_f}{\mu_{thnf}}\frac{\sigma_{thnf}}{\sigma_f}\right)f' + \frac{\mu_f}{\mu_{thnf}}\frac{(\rho\beta)_{thnf}}{(\rho\beta)_f}\xi^{-1}\alpha\theta + \\ + \frac{\rho_{thnf}}{\rho_f}\frac{\mu_f}{\mu_{thnf}}ff'' - \frac{\rho_{thnf}}{\rho_f}\frac{\mu_f}{\mu_{thnf}}f'^2 = 0, \tag{12}$$

$$\frac{1}{\mathrm{Pr}}\left(\frac{k_{thnf}}{k_f}+R_d\right)\theta'' + \mathrm{Ec}\xi^2\frac{\mu_{thnf}}{\mu_f}f''^2 + \\ + \frac{k_{thnf}}{k_f}\frac{\rho_{thnf}}{\rho_f}\frac{\mu_f}{\mu_{thnf}}\frac{\mathrm{Ec}}{\mathrm{Pr}}[E^*f' + F^*\theta] + \\ + \mathrm{Ec}\xi^2\left(\lambda\frac{\mu_{thnf}}{\mu_f} + M\frac{\sigma_{thnf}}{\sigma_f}\right)f'^2 + \frac{(\rho c_p)_{thnf}}{(\rho c_p)_f}f\theta' = 0, \tag{13}$$

with related boundary conditions:

– at η =0:

$$f' = 1, \qquad f = 0, \qquad \theta = 1, \tag{14a}$$

– as $\eta \to \infty$:

$$f' \to 0, \qquad \theta \to 0. \tag{14b}$$

5.2. Second-level truncation

Introducing new variables $g = \partial f/\partial\xi$ and $h = \partial\theta/\partial\xi$, and differentiating Eqs. (6)−(8) over ξ, and assuming $\xi \ll 1$, yields:

$$g''' - \left(\lambda + M\frac{\mu_f}{\mu_{thnf}}\frac{\sigma_{thnf}}{\sigma_f}\right)g' + \frac{\mu_f}{\mu_{thnf}}\frac{(\rho\beta)_{thnf}}{(\rho\beta)_f}\xi^{-1}\alpha(h - \xi^{-1}\theta) + \\ + \frac{\rho_{thnf}}{\rho_f}\frac{\mu_f}{\mu_{thnf}}(2gf'' + fg'') - 3\frac{\rho_{thnf}}{\rho_f}\frac{\mu_f}{\mu_{thnf}}f'g' + \\ - \frac{\mu_f}{\mu_{thnf}}\frac{\rho_{thnf}}{\rho_f}\xi(g'^2 - gg'') = 0, \tag{15}$$

$$\frac{1}{\mathrm{Pr}}\left(\frac{k_{thnf}}{k_f}+R_d\right)h'' + 2\mathrm{Ec}\xi\frac{\mu_{thnf}}{\mu_f}f''^2 + 2\mathrm{Ec}\xi^2\frac{\mu_{thnf}}{\mu_f}f''g'' + \\ + \frac{k_{thnf}}{k_f}\frac{\rho_{thnf}}{\rho_f}\frac{\mu_f}{\mu_{thnf}}\frac{\mathrm{Ec}}{\mathrm{Pr}}[E^*g' + F^*h] + \\ + 2\mathrm{Ec}\xi\left(\lambda\frac{\mu_{thnf}}{\mu_f} + M\frac{\sigma_{thnf}}{\sigma_f}\right)f'^2 + \\ + 2\mathrm{Ec}\xi^2\left(\lambda\frac{\mu_{thnf}}{\mu_f} + M\frac{\sigma_{thnf}}{\sigma_f}\right)f'g' + \\ + \frac{(\rho c_p)_{thnf}}{(\rho c_p)_f}(fh' + 2g\theta' - f'h) - \frac{(\rho c_p)_{thnf}}{(\rho c_p)_f}\xi[g'h - gh'] = 0, \tag{16}$$

with related boundary conditions:

– at η =0:

$$g' = 0, \qquad g = 0, \qquad h = 0, \tag{17a}$$

– as $\eta \to \infty$:

$$g' \to 0, \qquad h \to 0\,. \tag{17b}$$

6. Results and discussion

Numerical solutions for the dimensionless partial differential equations (Eqs. (6) and (7)) and the designated boundary conditions (Eqs. (8a), (8b)) are meticulously derived using the local non-similarity method, which is implemented up to a second truncation level with the bvp4c MATLAB toolkit. This study investigates the influence of the magnetic number and porosity parameter in a porous medium containing various working fluids, including Al_2O_3 + water, Al_2O_3 + TiO_2 + water, and Al_2O_3 + TiO_2 + MgO + water. The properties of water, aluminium oxide, titanium oxide and magnesium oxide, the models of thermophysical properties, and computed values of $\mathrm{Re}^{1/2}C_f$ and $\mathrm{Re}^{-1/2}\mathrm{Nu}$ are shown in Tables 1−4, respectively.

Table 1. Properties of the water, aluminium oxide (Al_2O_3), titanium oxide (TiO_2) and magnesium oxide (MgO) [30,33].

Materials	ρ, kg/m³	K, W/(m·K)	σ, Ωm	β, 1/K	c_p, J/(kg·K)
Aluminium oxide (Al_2O_3)	3970	40	$35\cdot10^{6}$	$0.85\cdot10^{-5}$	765
Titanium oxide (TiO_2)	4250	8.9538	$1\cdot10^{-12}$	$0.9\cdot10^{-5}$	686.6
Magnesium oxide (MgO)	3560	45	$2.6\cdot10^{6}$	$1.05\cdot10^{-5}$	955
Water (H_2O)	997.1	0.613	$5.5\cdot10^{-6}$	$21\cdot10^{-5}$	4179

To evaluate the proposed methods' effectiveness and precision, an extensive comparison was made between the computational results and the findings of several esteemed authors, as shown in Table 5:

– Tsai et al. [35] utilised the Chebyshev finite difference method, whereas Gireesha et al. [36] applied the Runge-Kutta-Fehlberg method for their solutions,
– the present research employs the local non-similarity method up to second-level truncation using the bvp4c MATLAB package.

Table 2. Models of thermo-physical properties [34].

Viscosity	$\mu_{(\mathrm{Al_2O_3+TiO_2+MgO})\mathrm{water}} = \dfrac{(\mathbf{Al_2O_3 + TiO_2})\mathbf{water}}{(1-\phi_{\mathrm{Al_2O_3}})^{2.5}(1-\phi_{\mathrm{TiO_2}})^{2.5}(1-\phi_{\mathrm{SiO_2}})^{2.5}}$
Density	$\rho_{(\mathrm{Al_2O_3+TiO_2+MgO})\mathrm{water}} = (1-\phi_{\mathrm{MgO}})\left((1-\phi_{\mathrm{TiO_2}})(1-\phi_{\mathrm{Al_2O_3}})\rho_{\mathrm{water}} + \phi_{\mathrm{Al_2O_3}}\rho_{\mathrm{Al_2O_3}} + \phi_{\mathrm{TiO_2}}\rho_{\mathrm{TiO_2}}\right) + \phi_{\mathrm{MgO}}\rho_{\mathrm{MgO}}$
Heat capacitance	$(\rho c_p)_{(\mathrm{Al_2O_3+TiO_2+MgO})\mathrm{water}} = (1-\phi_{\mathrm{MgO}})\left((1-\phi_{\mathrm{TiO_2}})\left((1-\phi_{\mathrm{Al_2O_3}})(\rho c_p)_{\mathrm{water}} + \phi_{\mathrm{Al_2O_3}}(\rho c_p)_{\mathrm{Al_2O_3}}\right) + \phi_{\mathrm{TiO_2}}(\rho c_p)_{\mathrm{TiO_2}}\right) + \phi_{\mathrm{MgO}}(\rho c_p)_{\mathrm{MgO}}$
Thermal expansion	$(\rho\beta)_{(\mathrm{Al_2O_3+TiO_2+MgO})\mathrm{water}} = (1-\phi_{\mathrm{MgO}})\left((1-\phi_{\mathrm{TiO_2}})\left((1-\phi_{\mathrm{Al_2O_3}})(\rho\beta)_{\mathrm{water}} + \phi_{\mathrm{Al_2O_3}}(\rho\beta)_{\mathrm{Al_2O_3}}\right) + \phi_{\mathrm{TiO_2}}(\rho\beta)_{\mathrm{TiO_2}}\right) + \phi_{\mathrm{MgO}}(\rho\beta)_{\mathrm{MgO}}$
Electric conductivity	$\dfrac{\sigma_{(\mathrm{Al_2O_3+TiO_2+MgO})\mathrm{water}}}{\sigma_{(\mathrm{Al_2O_3+TiO_2})\mathrm{water}}} = \dfrac{\sigma_{\mathrm{MgO}} + 2\sigma_{(\mathrm{Al_2O_3+TiO_2})\mathrm{water}} - 2\phi_{\mathrm{MgO}}(\sigma_{(\mathrm{Al_2O_3+TiO_2})\mathrm{water}} - \sigma_{\mathrm{MgO}})}{\sigma_{\mathrm{MgO}} + 2\sigma_{(\mathrm{Al_2O_3+TiO_2})\mathrm{water}} + \phi_{\mathrm{MgO}}(\sigma_{(\mathrm{Al_2O_3+TiO_2})\mathrm{water}} - \sigma_{\mathrm{MgO}})}$
Thermal conductivity	$\dfrac{k_{(\mathrm{Al_2O_3+TiO_2+SiO_2})\mathrm{water}}}{k_{(\mathrm{Al_2O_3+TiO_2})\mathrm{water}}} = \dfrac{k_{\mathrm{MgO}} + 2k_{(\mathrm{Al_2O_3+TiO_2})\mathrm{water}} - 2\phi_{\mathrm{MgO}}(k_{(\mathrm{Al_2O_3+TiO_2})\mathrm{water}} - k_{\mathrm{MgO}})}{k_{\mathrm{MgO}} + 2k_{(\mathrm{Al_2O_3+TiO_2})\mathrm{water}} + \phi_{\mathrm{MgO}}(k_{(\mathrm{Al_2O_3+TiO_2})\mathrm{water}} - k_{\mathrm{MgO}})}$

Table 3. Computed values of $\mathrm{Re}^{1/2}C_f$ for various values of M, λ, α.

M	λ	α	$\mathrm{Re}^{1/2}C_f$		
			Al_2O_3	$Al_2O_3 + TiO_2$	$Al_2O_3 + TiO_2 + MgO$
0.3	0.3	0.5	−1.5432014126	−1.2943728742	−1.0885117924
0.5			−1.9414080301	−1.6095879270	−1.3361500205
0.7			−2.2746152535	−1.8755502640	−1.5468988871
0.5	0.3	0.5	−1.9414080301	−1.6095879270	−1.3361500205
	0.6		−1.9727973884	−1.6471243162	−1.3809461220
	1.0		−2.0139344766	−1.6959626978	−1.4386415544
		0.5	−1.9414080301	−1.6095879270	−1.3361500205
		1.0	−1.8650650802	−1.5466559231	−1.2855071000
		1.5	−1.2312155521	−1.4788166666	−1.7825933276

Table 4. Computed values of $\mathrm{Re}^{-1/2}\mathrm{Nu}$ for various values of M, λ, α, R_d, Ec, E^* and F^*; $\phi_{\mathrm{Al_2O_3}} = \phi_{\mathrm{TiO_2}} = \phi_{\mathrm{MgO}} = 0.1$

M	λ	R_d	Ec	E^*	F^*	$\mathrm{Re}^{-1/2}\mathrm{Nu}$		
						Al_2O_3 + water	$Al_2O_3 + TiO_2$ + water	$Al_2O_3 + TiO_2 + MgO$ + water
0.5	0.3	1.0	0.2	0.1	0.1	−0.6979895966	−0.6954793018	−0.7170713161
1.0						−0.7986160421	−0.7536400412	−0.7074828826
1.5						−0.8978679485	−0.8674086293	−0.8187923402
	0.3					−0.6979895966	−0.6954793018	−0.7170713161
	0.6					−0.5307828279	−0.6580774445	−0.6715155841
	1.0					−0.4997764931	−0.6145833652	−0.6192276302
		0.5				−0.4894079681	−0.4841726931	−0.5147548449
		1.0				−0.6979895966	−0.6954793018	−0.7170713161
		1.5				−0.8494338404	−0.8480060767	−0.8649297428
			0.2			−0.6979895966	−0.6954793018	−0.7170713161
			0.3			−0.6820049371	−0.6787217611	−0.6885904197
			0.4			−0.6661576762	−0.6620799098	−0.6601762966
				0.1		−0.6979895966	−0.6954793018	−0.7170713161
				0.3		−0.7154796303	−0.7148261966	−0.7170661331
				0.5		−0.7328774635	−0.7340835802	−0.7170609501
					0.1	−0.6979895966	−0.6954793018	−0.7170713161
					0.3	−0.7083172021	−0.7064924464	−0.7170685399
					0.5	−0.7185305620	−0.7173727386	−0.7170657638

Table 5. The comparison of dimensionless temperature gradient $\theta'(0)$ for the case of $M = \lambda = \alpha = \mathrm{Ec} = R_d = E^* = 0$ and $\phi_{\mathrm{Al_2O_3}} = \phi_{\mathrm{TiO_2}} = \phi_{\mathrm{MgO}} = 0$.

Pr	F^*	Tsai et al. [36], Chebyshev finite difference method	Gireesha et al. [37], Runge-Kutta-Fehlberg method	Present study, local non-similarity method
2	−2	−2.4859	−2.4859	−2.4860961811
3	−3	−3.0281	−3.0281	−3.0730949222
4	−4	−3.5851	−3.5851	−3.5679155162

The influence of the buoyancy parameter α on the velocity, represented by $\frac{\partial f}{\partial \eta}(\xi,\eta)$, in the context of nanoparticle presence, is vividly illustrated in Fig. 2.

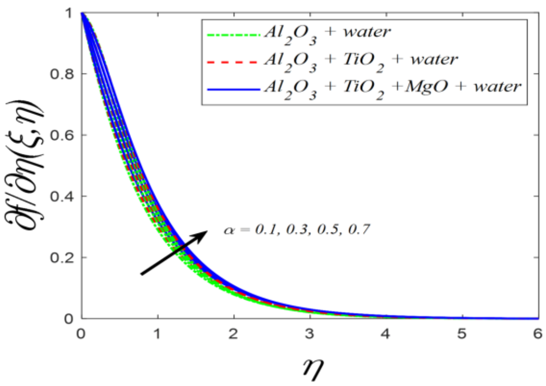

Fig. 2. The effect of buoyancy parameter α on velocity profile; $\lambda = 0.1$, $M = 1.0$, $E^* = F^* = 0.5$, $R_d = 1.3$ and Ec = 0.1.

Notably, the figure conspicuously elucidates that augmenting the value of α leads to a discernible escalation in the fluid velocity $\frac{\partial f}{\partial \eta}(\xi,\eta)$. Furthermore, the thickness of the momentum boundary layer was observed to increase as the values of the buoyancy parameter δ were enhanced. Variations in δ correspond to variations in distance from the surface. The data indicate that the buoyancy force acting as an assistive factor exhibits characteristics like those of a favourable pressure gradient. The buoyancy force has a significant impact on the movement of liquid through a consolidated permeable medium. Al_2O_3 + TiO_2 + MgO + water, in comparison to Al_2O_3 + TiO_2 + water, is more sensitive to changes in the buoyancy parameter.

Figures 3a and 3b illustrate the impact of λ on the distribution of three types of nanofluids: Al_2O_3 + TiO_2 + MgO + water, Al_2O_3 + TiO_2 + water, and Al_2O_3 + water. As the value of λ is increased, there is a decrease in velocity $\frac{\partial f}{\partial \eta}(\xi,\eta)$ while the thermal profile $\theta(\xi,\eta)$ rises. From a physical standpoint, the presence of a permeable medium results in an increase in flow resistance, leading to a reduction in both flow velocity and flow rate. Consequently, the fluid's temperature rises because of the heating sheet's energy transfer to the medium. Therefore, the thickness of the boundary layer decreases as a function of the surface layer's velocity. The resultant layer gradually thins out. The velocity distribution is observed to be greater for Al_2O_3 + water and lesser for Al_2O_3 + TiO_2 + MgO + water, whereas the temperature profile exhibits an opposite trend.

Figures 4a and 4b demonstrate the influence of the magnetic number (M) on the distributions of velocity $\frac{\partial f}{\partial \eta}(\xi,\eta)$ and temperature $\theta(\xi,\eta)$ in Al_2O_3 + TiO_2 + MgO + water, Al_2O_3 + TiO_2 + water, and Al_2O_3 + water.

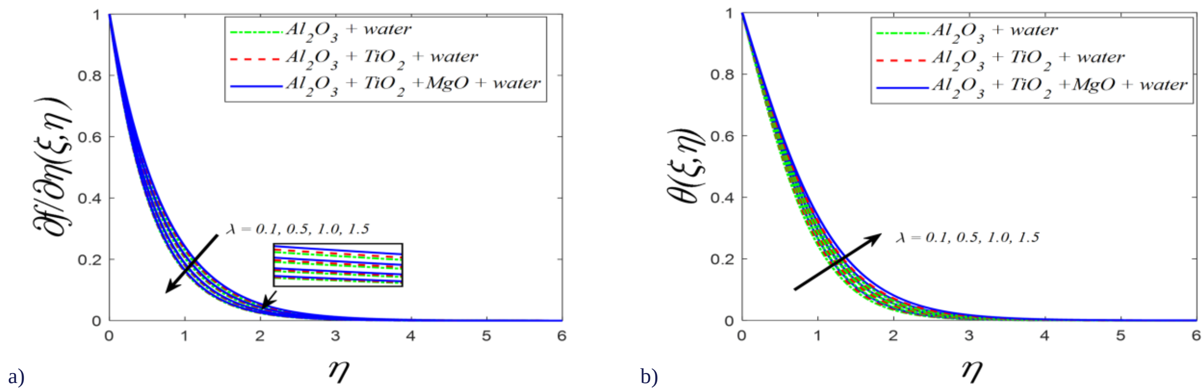

Fig. 3. The effect of porosity parameter λ on (a) velocity and (b) temperature profile; $\alpha = 0.1$, $M = 1.0$, $E^* = F^* = 0.5$, $R_d = 1.3$ and Ec = 0.1.

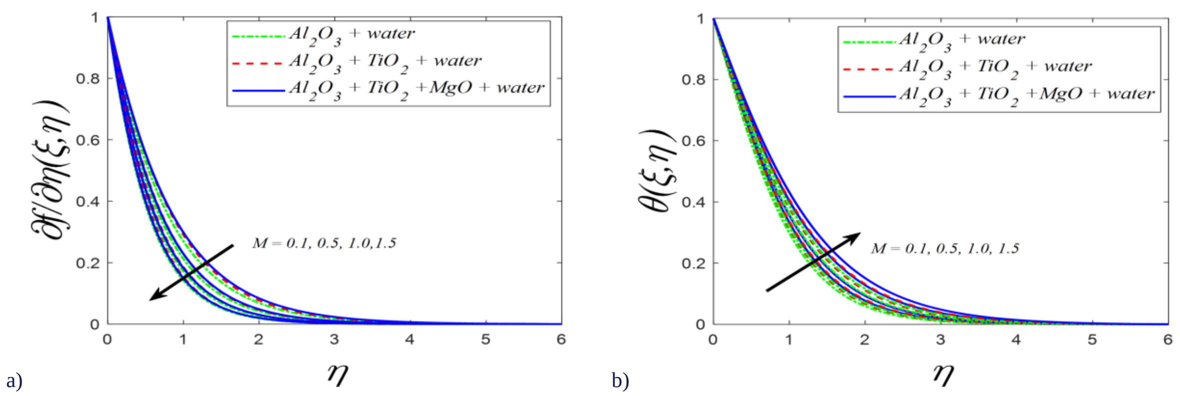

Fig. 4. The effect of magnetic number M on (a) velocity and (b) temperature profile; $\alpha = 0.1$, $\lambda = 0.1$, $E^* = F^* = 0.5$, $R_d = 1.3$ and Ec = 0.1.

As M increases with time, the temperature of the nanofluid also increases; on the other hand, the velocity distributions are found to decrease. The magnetic field is applied outside the fluid and perpendicular to the fluid flow, and its effect on the velocity and temperature of nanoparticles in the fluid is evaluated. The Lorentz force, which occurs due to the magnetic field, provides resistance which impedes and decelerates the movement of fluid particles and consequently decreases fluid velocity. The resistance force caused by the magnetic field reinforcement increases the thickness of the boundary layer and the density of nanoparticles. Consequently, the temperature distribution becomes more pronounced. When M increases, the nanofluid exhibits an increase in velocity. Both Al_2O_3 + TiO_2/water and Al_2O_3 + TiO_2 + MgO/water exhibit an elevated temperature profile. Furthermore, the temperature distribution for the ternary Al_2O_3 + TiO_2 + MgO/water nanofluid increases more noticeably than that of Al_2O_3 + TiO_2/water and Al_2O_3/water nanofluids.

Figures 5 and 6 have been created to investigate the impact of heating sources (sinks) E^* and F^* on the temperature field $\theta(\xi, \eta)$.

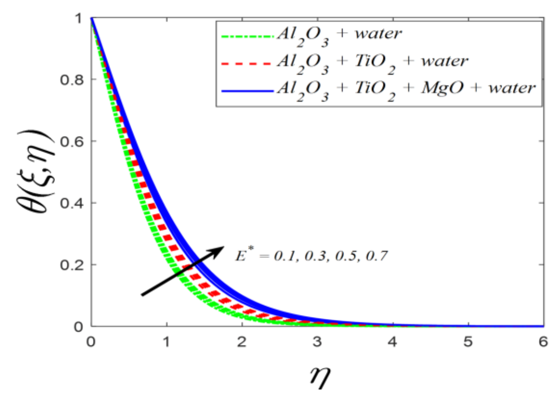

Fig. 5. The effect of E^* on the temperature profile; α = 0.1, λ = 0.1, M = 1.0, F^* = 0.5, R_d = 1.3 and Ec = 0.1.

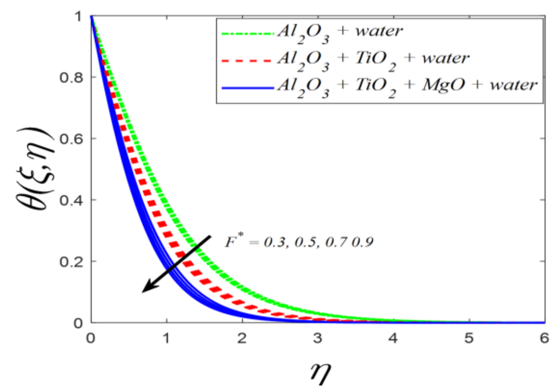

Fig. 6. The effect of F^* on the temperature profile; α = 0.1, λ = 0.1, M = 1.0, E^* = 0.5, R_d = 1.3 and Ec = 0.1.

It is a well-established fact that, in the case of heat absorption E^*, liquid shifts away from the surface and moves towards the wall in a vertical direction in the case of heat generation F^*. The system absorbs heat in the state of E^*. Both E^* and F^* operate based on the premise of an endothermic or exothermic reaction, where the scheme either absorbs or releases heat. The process of photosynthesis is a prime example of heat absorption, wherein plants absorb heat to synthesise their food. The nuclear fission reaction exemplifies a phenomenon of heat generation whereby heat is released through a specific process. The increase in volume fraction of nanoparticles leads to an increase in intermolecular collisions among fluid molecules, resulting in a corresponding change in fluid properties. The distribution of thermal conductivity and temperature is uniform throughout the fluid flowing in an upward direction. The upward change is more prominent in the case of Al_2O_3 + TiO_2 + MgO + water compared to Al_2O_3 + TiO_2 + water and Al_2O_3 + water, as depicted in Fig. 5. It has been observed that there is an inverse relationship between the thickness of a fluid and its temperature. It has been observed that an increase in fluid viscosity results in a decrease in fluid temperature, which causes more heat to be released. This ultimately leads to a reduction in fluid temperature in the event of an increase in F^*, as depicted in Fig. 6.

Figure 7 elucidates the significant effects of thermal radiation on the temperature distributions in Al_2O_3 + TiO_2 + MgO + water, Al_2O_3 + TiO_2 + water, and Al_2O_3 + water, where temperature increments scale linearly with the radiation parameter R_d, highlighting radiation as a dominant heat transfer pathway that extracts energy from the vibrational and translational kinetics of liquid particles to generate thermal energy through fluid agitation and consequent heating. This mechanism is expected to increase nanoparticle concentrations in the boundary layer according to radiation intensity, causing localised heat buildup.

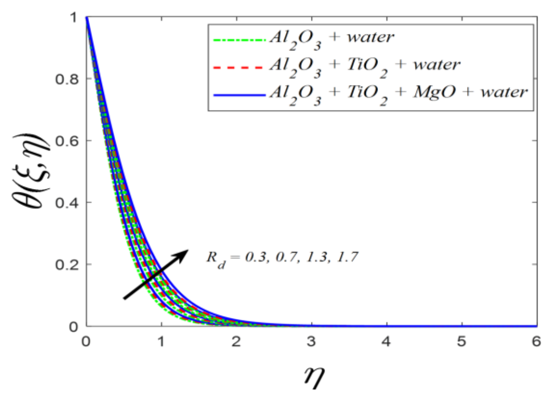

Fig. 7. The effect of R_d on the temperature profile; α = 0.1, λ = 0.1, M = 1.0, E^* = F^* = 0.5 and Ec = 0.1.

Graphical data substantiate that nanofluids exhibit the greatest thermal affinity, exceeding Al_2O_3 + water and Al_2O_3 + TiO_2 + water and Al_2O_3 + TiO_2 + MgO + water in heat retention, unlocking myriad applications across industries: in solar thermal systems, nanoparticle-water enhancements could propel collector efficiencies via superior radiative uptake in sun-rich environments, fostering sustainable energy transitions; electronics cooling benefits from hybrid nanofluid boundary layer synergies in microchannel designs, averting thermal failures in compact devices.

The impact of the Eckert number Ec on the temperature distribution is illustrated in Fig. 8.

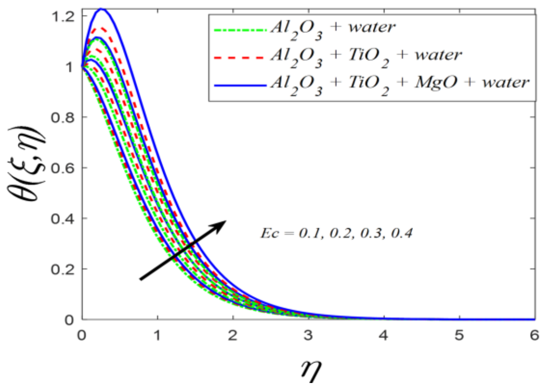

Fig. 8. The effect of Ec on the temperature profile; $\alpha = 0.1$, $\lambda = 0.1$, $M = 1.0$, $E^* = F^* = 0.5$, $R_d = 1.3$.

Empirical evidence clearly shows that better results occur as water temperatures rise. The generation of frictional heating has been attributed to the amplification in question, as per recent findings. The ratio of the difference in kinetic energy to the change in enthalpy between a solid boundary and a fluid is quantified by the Eckert number, which is a nondimensional quantity. Any kind of fluid may have its kinetic energy transformed into stored energy using a newly proposed process. This process is achieved through the performance of work against viscous strains incrementally. This phenomenon is observable. The figure illustrates that the impact of $Al_2O_3 + TiO_2 + MgO$ + water on temperature distribution is more significant in comparison to that of $Al_2O_3 + TiO_2$ + water and Al_2O_3 + water.

6. Conclusions

This current study endeavours to assess the influence of thermal radiation and Ohmic heating on the mixed convection boundary-layer flow of a magnetised nanofluid over a horizontal surface. This surface is situated within a porous medium and is under steady-state conditions. The governing boundary layer equations undergo a process of non-dimensionalisation, leading to the emergence of a challenging system of nonlinear partial differential equations. The equations are then solved using numerical solution methods in MATLAB, which are based on the powerful nature of the bvp4c toolset and instead use the local non-similarity technique to do so. The parameters which influence the flow and heat transfer characteristics have been explained in the study, including λ, α, M and R_d. According to the results of the present research, it is possible to draw the following conclusions:

1. The precision and verification of the present study have been provided in tabular format, as compared to the previous literature published, which used different numerical techniques and methods.
2. The graphs indicate the influence of M on the velocity and temperature profile. As the magnetic number increases, the velocity profile decreases and the heat profile increases. The velocity profile also decreases more with $Al_2O_3 + TiO_2 + MgO$ + water compared to $Al_2O_3 + TiO_2$ + water and Al_2O_3 + water, and more control is exerted by $Al_2O_3 + TiO_2 + MgO$ + water. Similarly, it is observed that the heat transfer rate is higher in both $Al_2O_3 + TiO_2$ + water and in Al_2O_3 + water, but the drag force is lower in $Al_2O_3 + TiO_2 + MgO$ + water.
3. The porosity parameter affects the thermal profile more for $Al_2O_3 + TiO_2 + MgO$ + water as compared to $Al_2O_3 + TiO_2$ + water and Al_2O_3 + water, which affects the velocity profile less. During an increase, the rate of heat transfer decreases, whereas the drag coefficient decreases more slowly in $Al_2O_3 + TiO_2 + MgO$ + water than in $Al_2O_3 + TiO_2$ + water.
4. As the values of R_d and Ec increase, the thermal profile and the rate of heat transfer become increased, but the influence of $Al_2O_3 + TiO_2 + MgO$ + water is much stronger than that of $Al_2O_3 + TiO_2$ + water and Al_2O_3 + water.

References

[1] Choi, S.U., & Eastman, J.A. (1995). Enhancing thermal conductivity of fluids with nanoparticles. *ASME International Mechanical Engineering Congress & Exposition, November 12−17, San Francisco, USA.* Rep. No. ANL/MSD/CP-84938; CONF-951135-29. doi: 10.1115/IMECE1995-0926

[2] Buongiorno, J. (2006). Convective transport in nanofluids. *Journal of Heat and Mass Transfer*, 128(3), 240−250. doi: 10.1115/1.2150834

[3] Mabood, F., Khan, W., & Ismail, A. (2015). MHD boundary layer flow and heat transfer of nanofluids over a nonlinear stretching sheet: A numerical study. *Journal of Magnetism and Magnetic Materials*, 374, 569−576. doi: 10.1016/j.jmmm.2014.09.013

[4] Siddiqui, B.K., Batool, S., ul Hassan, Q.M., & Malik, M.Y. (2021). Irreversibility analysis in the boundary layer MHD two dimensional flow of Maxwell nanofluid over a melting surface. *Ain Shams Engineering Journal*, 12(3), 3217−3227. doi: 10.1016/j.asej.2021.01.017

[5] Masood, S., Farooq, M., & Anjum, A. (2021). Influence of heat generation/absorption and stagnation point on polystyrene–TiO2/H2O hybrid nanofluid flow. *Scientific Reports*, 11(1), 22381. doi: 10.1038/s41598-021-01747-9

[6] Hussain, I., Hobiny, A., Irfan, M., Tabrez, M., & Khan, W. (2023). Impact of magnetic dipole contribution on radiative ferromagnetic Cross nanofluid with viscous dissipation aspects. *Journal of Magnetism and Magnetic Materials*, 579, 170706. doi: 10.1016/j.jmmm.2023.170706

[7] Chen, T.S., Sparrow, E.M., & Mucoglu, A. (1977). Mixed convection in boundary layer flow on a horizontal plate. *Journal of Heat and Mass Transfer*, 99(1), 66−71. doi: 10.1115/1.3450657

[8] Chamkha, A.J., Al-Mudhaf, A.F., & Pop, I. (2006). Effect of heat generation or absorption on thermophoretic free convection boundary layer from a vertical flat plate embedded in a porous medium. *International Communications in Heat and Mass Transfer*, 33(9), 1096−1102. doi: 10.1016/j.icheatmasstransfer.2006.04.009

[9] Ahmad, S., & Pop, I. (2010). Mixed convection boundary layer flow from a vertical flat plate embedded in a porous medium filled with nanofluids. *International Communications in Heat and Mass Transfer*, 37(8), 987−991. doi: 10.1016/j.icheatmasstransfer.2010.06.004v

[10] Mahanthesh, B., Gireesha, B.J., & Animasaun, I.L. (2018). Exploration of non-linear thermal radiation and suspended nanoparticles effects on mixed convection boundary layer flow of nanoliquids on a melting vertical surface. *Journal of Nanofluids*, 7(5), 833−843. doi: 10.1166/jon.2018.1521v

[11] Cao, W., Animasaun, I.L., Yook, S.J., Oladipupo, V.A., & Ji, X. (2022). Simulation of the dynamics of colloidal mixture of water with various nanoparticles at different levels of partial slip: Ternary-hybrid nanofluid. *International Communications in Heat and Mass Transfer*, 135, 106069. doi: 10.1016/j.icheatmasstransfer.2022.106069

[12] Jakeer, S., Reddy, S.R.R., Rashad, A.M., Rupa, M.L., & Manjula, C. (2023). Nonlinear analysis of Darcy-Forchheimer flow in EMHD ternary hybrid nanofluid (Cu-CNT-Ti/water) with radiation effect. *Forces in Mechanics*, 10, 100177. doi: 10.1016/j.finmec.2023.100177

[13] Lauriat, G., & Prasad, V. (1987). Natural convection in a vertical porous cavity: a numerical study for Brinkman-extended Darcy formulation. *Journal of Heat and Mass Transfer*, 109(3), 688−696. doi: 10.1115/1.3248143

[14] Beckermann, C., Viskanta, R., & Ramadhyani, S. (1986). A numerical study of non-Darcian natural convection in a vertical enclosure filled with a porous medium. *Numerical Heat Transfer*, 10(6), 557−570. doi: 10.1080/10407788608913535

[15] Cortell, R. (2005). Flow and heat transfer of a fluid through a porous medium over a stretching surface with internal heat generation/absorption and suction/blowing. *Fluid Dynamics Research*, 37(4), 231−245. doi: 10.1016/j.fluiddyn.2005.05.001

[16] Salahuddin, T., Akram, A., Khan, M., Siddique, N., Alaoui, M.K., & Aly, S. (2020). A comparative study of γAl2O3–C2H6O2 and γAl2O3–H2O near a vertical curved surface having porous medium. *International Journal of Hydrogen Energy*, 45(46), 24275−24284. doi: 10.1016/j.ijhydene.2020.06.120

[17] Hussain, M., Rahim, I., Jan, A., Ahmad, M., & Khan, M.R. (2025). Comparative analysis of the radiative stagnation point nanofluid flow with the considerations of inclined magnetic field and porous medium. *Journal of Thermal Analysis and Calorimetry*, 150, 22597–22605. doi: 10.1007/s10973-025-15219-z

[18] Keshavarzian, B., & Sayehvand, H.O. (2023). Validation of the local thermal equilibrium assumption for free convection boundary layer flow over a horizontal cylinder embedded in an infinite saturated porous medium. *Results in Physics*, 44, 106112. doi: 10.1016/j.rinp.2022.106112

[19] Sparrow E.M., & Cess, R.D. (1961). The effect of a magnetic field on free convection heat transfer. *International Journal of Heat and Mass Transfer*. 3(4), 267–274. doi: 10.1016/0017-9310(61)90042-4

[20] Ellahi, R., Alamri, S.Z., Basit, A., & Majeed, A. (2018). Effects of MHD and slip on heat transfer boundary layer flow over a moving plate based on specific entropy generation. *Journal of Taibah University for Science*, 12(4), 476−482. doi: 10.1080/16583655.2018.1483795

[21] Jan, A., Ahmad, A., & Aslam, F. (2025). Enhanced thermal performance of aggregated TiO_2 nanoparticles in non-Newtonian fluid flow over curved surfaces under magnetic and porous medium effects. *Journal of Thermal Analysis and Calorimetry*, 150(18), 14517−14529. doi: 10.1007/s10973-025-14516-x

[22] Iqbal, J., & Abbasi, F.M. (2026). Analysis of entropy generation for Magnetohydrodynamics peristaltic motion of Carreau-Yasuda nanofluid through a curved channel with variable thermal conductivity and Joule heating. *Waves in Random and Complex Media*, 35(7), 12563–12582. doi: 10.1080/17455030.2022.2134603

[23] Ghasemi, S.E., Mohsenian, S., Gouran, S., & Zolfagharian, A. (2022). A novel spectral relaxation approach for nanofluid flow past a stretching surface in presence of magnetic field and nonlinear radiation. *Results in Physics*, 32, 105141. doi: 10.1016/j.rinp.2021.105141

[24] Iqbal, J., Abbasi, F.M., Alkinidri, M., & Alahmadi, H. (2023). Heat and mass transfer analysis for MHD bioconvection peristaltic motion of Powell-Eyring nanofluid with variable thermal characteristics. *Case Studies in Thermal Engineering*, 43, 102692. doi: 10.1016/j.csite.2022.102692

[25] Sparrow, E.M., Quack, H., & Boerner, C.J. (1970). Local nonsimilarity boundary-layer solutions. *AIAA Journal*, 8(11), 1936−1942. doi: 10.2514/3.6029

[26] Sparrow, E.M., & Yu, H.S. (1971). Local non-similarity thermal boundary-layer solutions. *ASME. Journal Heat and Mass Transfer*, 93(4), 328–334. doi: 10.1115/1.3449827

[27] Jan, A., Farooq, U., Khan, M.I., & Aslam, F. (2025). Applications of neural networking analysis on drag reduction and heat transfer rate of non-Newtonian fluid flows in energy storage systems. *International Communications in Heat and Mass Transfer*, 169, 109569. doi: 10.1016/j.icheatmasstransfer.2025.109569

[28] Riaz, S., Naheed, N., Farooq, U., Lu, D., & Hussain, M. (2023). Non-similar investigation of magnetized boundary layer flow of nanofluid with the effects of Joule heating, viscous dissipation and heat source/sink. *Journal of Magnetism and Magnetic Materials*, 574, 170707. doi: 10.1016/j.jmmm.2023.170707

[29] Anuar, N.S., Bachok, N., & Pop, I. (2021). Influence of buoyancy force on Ag-MgO/water hybrid nanofluid flow in an inclined permeable stretching/shrinking sheet. *International Communications in Heat and Mass Transfer*, 123, 105236. doi: 10.1016/j.icheatmasstransfer.2021.105236

[30] Iqbal, Z., & Mehmood, Z. (2017). Elastic deformation analysis on MHD viscous dissipative flow of viscoelastic fluid: An exact approach. *Communications in Theoretical Physics*, 67(5), 561. doi: 10.1088/0253-6102/67/5/561

[31] Chamkha, A.J., Rashad, M., & Subba Reddy Gorla, R. (2014). Non-similar solutions for mixed convection along a wedge embedded in a porous medium saturated by a non-Newtonian nanofluid: natural convection dominated regime. *International Journal of Numerical Methods for Heat & Fluid Flow*, 24(7), 1471−1486. doi: 10.1108/HFF-07-2012-0169

[32] Jan, A., Khan, M.I., Farooq, U., Aslam, F., & Adnan, R. (2026). PINN-based numerical modeling of MHD flows in porous media over linear stretching boundaries. *International Communications in Heat and Mass Transfer*, 172, 110592. doi: 10.1016/j.icheatmasstransfer.2026.110592

[33] Rajesh, V., Mallesh, M.P., & Bég, O.A. (2015). Transient MHD free convection flow and heat transfer of nanofluid past an impulsively started vertical porous plate in the presence of viscous dissipation. *Procedia Materials Science*, 10, 80−89. doi: 10.1016/j.mspro.2015.06.028v

[34] Adnan, & Ashraf, W. (2022). Thermal efficiency in hybrid (Al_2O_3-CuO/H_2O) and ternary hybrid nanofluids (Al_2O_3-CuO-Cu/H_2O) by considering the novel effects of imposed magnetic field and convective heat condition. *Waves in Random and Complex Media*, 35(4), 8029-8044. doi: 10.1080/17455030.2022.2092233

[35] Tsai, R., Huang, K.H., & Huang, J.S. (2008). Flow and heat transfer over an unsteady stretching surface with non-uniform heat source. *International Communications in Heat and Mass Transfer*, 35(10), 1340−1343. doi: 10.1016/j.icheatmasstransfer.2008.07.001

[36] Gireesha, B.J., Ramesh, G.K., Abel, M.S., & Bagewadi, C.S. (2011). Boundary layer flow and heat transfer of a dusty fluid flow over a stretching sheet with non-uniform heat source/sink. *International Journal of Multiphase Flow*, 37(8), 977−982. doi: 10.1016/j.ijmultiphaseflow.2011.03.014